ISSN 0915-633X

# NATIONAL INSTITUTE FOR FUSION SCIENCE

## $CO_2$ Laser Diagnostics for Measurements of the Plasma Density Profile and Plasma Density Fluctuations on LHD

L.N. Vyachenslavov, K. Tanaka, K. Kawahata

(Received - Sep. 27, 1999 )

NIFS-694 Apr. 2001



RESEARCH REPORT
NIFS Series

TOKI, JAPAN

# $CO_2$ Laser Diagnostics for Measurements of the Plasma Density Profile and Plasma Density Fluctuations on LHD

L.N. Vyacheslavov*, K. Tanaka**, K. Kawahata**

* *Budker Institute of Nuclear Physics, , 630090, Novosibirsk, RUSSIA*
** *National Institute for Fusion Science,322-6,Oroshi,Toki, 509-5292,Japan*

**Abstract**

A $CO_2$ laser based diagnostics complimentary to the existing FIR interferometer is proposed. It combines interferometry for plasma density profile measurement under conditions of large density gradients, and both imaging and scattering techniques for observation of plasma fluctuations. Two-colour interferometer with a slab-like probe beam and a single multichannel linear detector array provide observation of plasma density profile and density fluctuations at two locations along the probe beam. Basic characteristics of the diagnostics are considered as well as some effects that include dispersion and are critical for two colour imaging technique. The results of the bench-top experiments with the prototype of the interferometer are presented.

Keywords: two-colour interferometer, plasma fluctuations, imaging techniques, diffraction, dispersion, Thomson scattering

## [1] Introduction

The multichord FIR interferometer system provides the main information about temporal evolution of the electron density profile and exhibits a good reliability during an operation on LHD [1]. The maximum electron density in the device is expected to be more than $10^{14}$ $cm^{-3}$ and can be accompanied by large density gradients near the plasma edge especially in the pellet injection discharges. The spatial resolution of the FIR interferometer, which is limited by diffraction, could be insufficient under these conditions. In the design of the FIR system a provision was made to incorporate a $CO_2$ laser interferometer, which becomes suitable for large density plasma. The $CO_2$ laser based imaging techniques have also well established capabilities in observation of plasma density fluctuations. The main goals of this paper is to consider some details of the multipurpose $CO_2$ laser diagnostics, which designed:

a) to operate in combination with FIR interferometer and to provide measurement of the plasma profile in regimes with large density gradients
b) to study plasma density fluctuations with spatial resolution and in interferometer, or phase contrast, or collective Thomson scattering modes

## [2] Plasma fluctuations parameters

Electrostatic drift waves are driven by gradients in plasma and are typically unstable over the significant fraction of the plasma cross section. Enhanced level of these waves can be source of anomalous transport. The range of unstable wave numbers $k_t$ ($cm^{-1}$), corresponding frequencies f (kHz), relative plasma density fluctuations $\delta Ne$ (%), wavelengths $\Lambda$ (cm), and parameter $k_t\rho_s$ [2] for LHD plasma are shown in Table I:

| $k_t$, $cm^{-1}$ | F, kHz | $\delta Ne$, % | $\Lambda$, cm | $k_t\rho_s$ |
|---|---|---|---|---|
| 0.27 | 24 | 7.3 | 23 | 0.05 |
| 0.67 | 60 | 3.0 | 9.3 | 0.12 |
| 1.1 | 100 | 1.7 | 5.5 | 0.21 |
| 1.7 | 140 | 1.2 | 3.8 | 0.3 |
| 2.2 | 190 | 0.9 | 2.8 | 0.41 |
| 2.8 | 240 | 0.71 | 2.2 | 0.51 |
| 3.4 | 280 | 0.58 | 1.8 | 0.63 |
| 4.1 | 330 | 0.49 | 1.5 | 0.75 |
| 4.8 | 370 | 0.42 | 1.3 | 0.87 |
| 5.5 | 420 | 0.37 | 1.1 | 1 |
| 6.2 | 460 | 0.32 | 1.0 | 1.1 |

Table 1 Parameters of electrostatic drift waves

Here $\rho_s = c_s/\omega_{ci}$, $v_e = c_s \cdot \frac{\rho_s}{L_n}$,

$$f = \frac{\omega_e}{2\pi\left(1 + \left(k_t \rho_s\right)^2\right)} + \frac{E_r\, k_t\, c}{2 \cdot \pi \cdot B}, \qquad (1)$$

$\omega_e = v_e k_t$ and plasma parameters used are Te = 2 keV, B = 2.5 T, $Ne = 5\,10^{13}$ $cm^{-3}$, $L_n = 50$ cm, $E_r = 10$ V/cm.

The second term in the equation for frequency corresponds to Doppler shift due to $\mathbf{E}_r$ x $\mathbf{B}$ drift of the plasma particles [3] with velocity $v_D = 4\,10^5$ cm/s for the given electric field. If this term dominants spatially resolved measurements of frequency of fluctuations can provide information about amplitude and fluctuations of electric field, which is important for study of anomalous transport and, vice verse, an a priory information about spatial structure of electric field can improve resolution along the viewing line for density fluctuations [4, 5].

Microturbulence with much shorter wavelength up to $c/\omega_{pe}$ and $r_{ci}$, which corresponds to wavelengths near 0.4cm under conditions used here, also can affect anomalous electron transport [6] and should be considered as a target for observations. It is worth to mention, though most of experiences in anomalous transport is obtained with tokamaks plasmas, to a great extent it could be applicable to processes in stellarators as well [7].

**[3]. The diagnostics layout**

Heterodyne interferometers perform very well in measurements of electron density profiles in fusion plasmas. They have advantages of self-calibration, no difficulties with phase passing through an extreme and with keeping at maximum sensitivity. Compensation of vibration on real devices is ordinarily provided utilizing two-color version of an interferometer. Improved spatial resolution is often accomplished recently by using slab or fan like probe beam instead of limited number of discrete probing beams [8]. Vibrations compensation can be achieved also in second harmonic or dispersion version of two color interferometer [9, 10]. This type of interferometer provides intrinsic phase compensation without any electronics and particularly good under limited accesses or room conditions. Yet, there is no known until now any experiment with extension of this system to the mid IR region.

For laser based diagnostics the situation with the technique for fluctuations measurements is relatively less obvious than with observation of density profiles. Generally accepted that wave scattering is better for short wavelength fluctuations while imaging techniques [11, 12] and far forward scattering [13] are preferable for long wavelength ones. Imaging interferometer [14] is able to sense fluctuations with wavelengths much larger than the probe beam diameter and it is its advantage over the phase contrast technique [11, 15, 16]. Obviously, k-space resolution is determined by the size of the beam waist in plasma in any case, so it is impossible to distinguish by mean of a single probe beam two waves with the wave vectors difference less than the resolution limit. The distinction between the interferometry with separate reference beam and the phase contrast method, which use zero order diffracted beam as reference one, is that the first method can detect the phase of fluctuations longer than resolution limit while the second can not. Several beams can improve resolution limit for the former type of imaging but cannot for the latter one. A lesser sensitivity to vibrations, which is the advantage of the phase contrast method, could be not crucial when a vibration-isolated stand and frame are available for an interferometer. Extremely precision phase counters, however, are necessary for heterodyne interferometers to perform as sensitive in observation of fluctuations as phase contrast instruments.

The basic idea of the project is to combine in a single instrument capabilities for observation both plasma density profile and plasma fluctuations. The schematic of the instrument is designed to be flexible in studying of fluctuation: with both imaging interferometric and phase contrast techniques as well as with the collective Thomson scattering method. Whereas all methods are principally line integrated there are ways to achieve spatial resolution along the viewing line. One way is to take the advantage of sheared magnetic field for resolution of fluctuation propagating normally to magnetic field [17, 18, 19]. Another approach to spatial resolution along the viewing line is the cross-correlation technique [20, 21]. The distinguished feature of our approach is employment of multichannel detection in crossed beam that permits simultaneous detection several z-locations of fluctuations instead of shot-to-shot scaning of cross point. We also suggest below the diagnostics version that enables simultaneous measurements both a density profile and fluctuations behavior in two spatial regions along the viewing direction using the magnetic shear. It is important that the further development of the diagnostic system towards the cross correlation technique needs no change in the schematic presented here but just addition of new elements.

The schematic view of the proposed diagnostics is presented in Fig.1. The diagram of the system is shown in Fig.2. We use the Mach-Zehnder type configuration instead of the Michelson one, which is typical for multi-chord interferometers. At the price of halved sensitivity to the plasma produced phase shift this way we achieve the spatial resolution required for imaging of the density fluctuation and plasma density profile. Diffraction (see also Section [4]B below) makes imaging with Michelson interferometer at the LHD scale impossible. Two probe cw lasers $CO_2$ and YAG are employed in two-color scheme of the heterodyne interferometer.

Most of optical equipment is situated in two shielded boxes (the laser box and the detectors box), which are located on the lower and upper part of the frame relatively, near the FIR interferometer optics. System uses 1-3 slab-like probe beams (a single-beam variant is presented in Figure 2). Each of the beams passes the vacuum chamber. The reference and local beams cross the divertor plasma. The FIR interferometer has one spatial channel to sense the

divertor plasma, which typically produces negligible phase shift even for FIR region.

The layout of diagnostics for main plasma is flexible. The configuration presented in Figure 2 includes single probe beam employed for scattering technique (linear array of detectors D1) and for imaging diagnostics of density profile (linear arrays D2 for 10μ radiation and and Si1 for 1μ radiation) and fluctuations (linear arrays D4). The parabolic mirror PM focuses the slab probe beam after it passed plasma onto Fourier transform plane. The beam splitters BS1 and BS2 separate the probe beam into three parts. In the Fourier transform plane of one of them is located linear array D1 used for Thomson scattering. This is the Thomson scattering part of the diagnostics. In the Fourier transform plane of the beam employed for observation of fluctuations either the slits SL for spatial filtration of the fluctuations image or phase plate for converting the interferometer into phase contrast instrument can be placed. In the later case the local beam is blocked in front of the array D4. The spatial filtration by the slit may be used for selection of particular range in the k-spectrum of signal. With the assumption that the direction of **k**-vector of phase fluctuations is normal to the direction of magnetic field, resolution in the direction of **k** can be used for spatially resolved along the viewing line observations in sheared magnetic field. In addition, selection of particular k in spectrum can simplify simultaneous observation of fluctuations of plasma density and plasma potential. For harmonic of fluctuations with particular k the amplitude and variation of the amplitude of phase signal gives amplitude and variation of density fluctuations with given k while the frequency of phase signal and variation of the frequency provide information on potential and its fluctuations. The imaging system for fluctuations can operate in two orthogonal polarization directions (see Fig. 3) that gives an additional capability for diagnostics. In the version presented in the figure two polarization directions permit simultaneous studying of the transversal behavior of fluctuations in two spatial points along the probe beam.

Employing λ/4 plates and polarization beam splitters PBS both in the probe and the local beams divides each beam into two beams with orthogonal polarization directions. The PBS in the probe beam is followed by two slits, which are situated in the Fourier transform planes and separate two spectral regions in a *k*-space. In case of the sheared magnetic field different directions of k correspond to different position in plasma along the probe beam. Then additional PBS combines two beams into single beam again. The reference beam also consists of two beams with two orthogonal directions of polarization. These beams are shifted in frequency by two acousto-optic modulators in a such a way that differences in frequency between the local beam and probe beam are 1 MHz for one of the polarization direction and 3 MHz for another. Figure 3 shows the diagram structure of polarization components for the probe ($Ep_x$, $Ep_y$) and the local ($Er_x$, $Er_y$) beams.

Linear array MCT 4 detects beating between the probe and the reference beams at two frequencies 1 and 3 MHz. Because detector is insensitive to polarization direction there is no signal at 2 MHz due to beating between two polarization of the local beam. As the MCT4 is situated in the image plane signals contains information about the spatial and time dependence of plasma fluctuations. The reference beam with detectors MCT3 and Si1 is used for account of most of uncompensated phase signal produced due to difference in the optical paths for two colors. A calibrated speaker can be placed in an appropriate point of either probe or reference beam to provide absolute sensitivity calibration and test of the entire systems for fluctuations measurement.

An appropriate electronics is needed to reveal the information on fluctuations. In the published literature an analog fast precise phase comparator with frequency range 0.01 – 40 MHz and resolution $10^{-4}$ fringe was reported [22] and a digital phase compurgator with frequency range 0.01 – 1 MHz [23] was applied for measurements of plasma fluctuations [24]. Important topic here is the frequency separation in twopolarization directions layout and an initial bandwidths of the laser outputs. Commercially available lasers both $CO_2$ and YAG have low enough bandwidth so acousto-optical modulators have not to increase it. Authors of publication [22] report about some problems with the spectral purity of modulated light while in Ref. 25 the beating signal is narrow enough.

The scattering part of the proposed diagnostics can operate relatively independently from the imaging system either in homodyne or in heterodyne modes. In the last case a fraction of the local beam is employed as it is shown in Fig. 2. It is possible also if the AOM4 produces for corresponding local beam a zero frequency shift relative to the probe beam. In this event the two polarization directions arrangement in the imaging part of the diagnostics can operate simultaneously also with zero frequency shift for one of polarization direction analogous to the phase contrast schema.

For observation of fluctuation we have to obtain localization along the beam axis. For this purpose we intend to modify the multi-channel interferometer for crossed beam correlation technique [20] or magnetic shear technique [17-19]. The crossed beam travels from lower port 1 to upper port 3 and has cross-points with port 2 beam as shown in fig.1. The crossed beam is injected the same port, where the vertical slab beam is injected, with small toroidal displacement.

## [4] Basic characteristics

### A. Sensitivity

For given parameters of an experiment

$Ne = 5\cdot10^{13}$ cm$^{-3}$, $\delta Ne = 10^{12}$ cm$^{-3}$, $L_{plasma} = 100$ cm, $\Lambda = 2$ cm, $\lambda1 = 10.6$ μm, $\lambda2 = 1.06$ μ,

the estimations of plasma produced shifts are as follows:

1. Phase shift produced by plasma bulk $\Delta\phi_b$:

$$\Delta\phi_b = r_e \cdot L_{plasma} \cdot \lambda1 \cdot Ne \cdot (1-x), \quad (2)$$

where $x = \lambda2/\lambda1$, $\Delta\phi_b = 1.3$ rad.

2. Phase shift due to randomly distributed fluctuations, $\Delta\phi_{fl}$ [26]:

$$\Delta\phi_{fl} = r_e \cdot \lambda1 \cdot \delta Ne \cdot \sqrt{\Lambda \cdot L_{plasma}}, \quad (3)$$

$\Delta\phi_{fl} = 4.2\times10^{-3}$ rad.

Relative phase shift caused by fluctuations:

$$\Delta\phi_{rel} = \sqrt{\frac{\Lambda}{L_{plasma}}} \cdot \frac{\delta Ne}{(Ne \cdot (1-x))}, \quad (4)$$

$\Delta\phi_{rel} = 3.2\times10^{-3}$

Sensitivity to the phase shift is determined by resolution of phase comparator that can be attained $10^{-4}$ fringe [22], by residual phase noise, and by noise of detection. The later can be made low enough for $LN_2$ cooled detectors to enable sensitivity limit of the imaging technique for fluctuations $\delta Ne = 6\cdot10^8$ cm$^{-3}$ under experimental conditions of ref. [27]. Another important parameter here is the ratio of saturation power to noise power for a detection system. This parameter characterizes the level of sensitivity to phase fluctuations relative to full level of the beating signal, which can be near the saturation limit. The ratio of saturation power to noise power was $4\cdot10^{12}$ in experiments on Tore Supra [25].

B. Resolution

Spatial resolution in the *transversal* direction is governed by number of detectors in the linear array and optical resolution, which needs precise optics and negligible diffraction effects. Diffraction puts the upper limit for fluctuation wave number to be observed with imaging technique at the distances large than field depth from the object plane as it follows from consideration in the next Section. The imaging optics should be precise enough not to limit the spatial resolution by producing distorted phase image of the object. The lower limit for k-resolution is settled by the largest seize in the Fourier plane, either the probe beam waist or the slit width:

$$\Delta K = (2\pi/(\lambda F)) \max(wp, d/2) \quad (5)$$

or in definitions reduced to the subject plane

$$\Delta K = 2/\min(wo, d_{eff}/\pi). \quad (6)$$

Here $d_{eff} = 2\lambda F/d$ is the size of slit diffraction pattern, $wp = F\lambda/(\pi wo)$ is the beam waist in the Fourier plane; wo is the beam waist in the subject plane, which is almost constant for wide collimated beam, and F is the focal length of the focusing system.

The spatial resolution in the *longitudinal* direction is governed by magnitude and gradient of magnetic shear and by angular resolution in a momentum space. The angular resolution depends in its turn on k-resolution in different directions. Slab-like probe beam leads to different k-resolution in directions along and normal to the slab longest side. The spatial resolution of the magnetic shear techniques obtained in Heliotron E experiment [18] was about the minor radius for $k \geq 0.4$mm$^{-1}$. For crossed beam correlation technique under LHD conditions the possible cross-angle $\theta_s$ is 4 5 degree. If some parts of port 2 beam and crossed beam, of which widths are d, are used for this schema as shown in fig. 2 (b), the spatial resolution becomes $\delta z = 2l_c/\tan\theta_s$ for $l_c > d$. Here $l_c$ is transverse to the magnetic field correlation length for fluctuations; $l_c$ is typically order of fluctuation wavelength for micro turbulence [11]. Minimum d is channel spacing, which is 5mm. So, the maximal k is $k \approx 2\pi/2d = 0.6$mm$^{-1}$. For maximum k and associated correlation length $l_c = 2d = 10$mm, the spatial resolution $\delta z$ is 254mm. This is one forth of the longer minor radius. Making channel spacing narrower, better spatial resolution for larger k is expected. The cross-points exist from edge to the center of plasma for slab beams simultaneously as shown in fig.2 (a). Unlike Surko's crossed beam schema [20], in the present technique it is possible to obtain spatial profile of fluctuation from a single shot without scanning cross points.

**[5] Dispersion effects**

Two-color heterodyne interferometer is much more resistant against variation of sensitivity or against parasitic change of optical paths than traditional interferometers. There still remain a few distortion effects that cannot be automatically compensated in two-color heterodyne system mostly because of dependence of these effects on wavelength. Below we consider some of them.

A. Thermal variation in refraction of optical elements

Two color arrangement enables effective compensation of change in length of optical passes produced by vibrations. Yet two-color technique is entirely incapable to compensate variations in optical length of dispersive elements, which is the case for all refractive optics. For example, thermal change in the refraction index and thickness of windows is different for two colors due to dispersion, so the associated phase shift can be confused with phase shift produced by plasma. Modification of refraction index of the windows due to heating of them by plasma emission and by high power microwaves during ECRH plasma is especially important in steady-state operation of LHD.

| characteristics | | ZnSe | $BaF_2$ | reference |
|---|---|---|---|---|
| Refraction index, n / temperature derivative, dn/dT [$10^{-6}$/°C] | λ, μm | | | [28] (ZnSe) [29] ($BaF_2$) |
| | 10.6 | 2.40/61 | 1.39/-14.1 | |
| | 9 3 | 2.41/61 | 1.41/-14.7 | |
| | 3.4 | 2.43/63 | 1 46/-15.5 | |
| | 1.3 | 2 47/68 | 1.47/-15.5 | |
| | 1.05 | 2.48/69.3 | 1.46/-15.4 | |
| Absorption index, k, $cm^{-1}$ $I = I_0 10^{-kl}$ | 2100 | 0.04 | no data | [30] |
| | 10.6 | no absorption | 0.12 | [31] |
| | 9.3 | no absorption | 0.04 | |
| Thermal expansion, $\alpha \times 10^6$ | | 7 | 18.4 | [32] |
| Thermoconductivity, λ, W/(cm K) | | 0.17 | 0.07 | [32, 33] |
| Specific heat, Cp, J/(g K) | | 0.35 | 0.41 | [32, 33] |
| Density ρ, $g/cm^3$ | | 5.2 | 4.8 | [32] |
| (Cpρ), $J/(cm^3 K)$ | | 1.9 | 1.97 | [32] |

Table 2. Thermal properties of ZnSe and $BaF_2$

The role that plays the above-mentioned effects depends on real features of window material. Typically ZnSe is employed because of its good transmission both in infrared and visible. Still $BaF_2$ also has attractive thermal properties to be considered as material for optics in interferometer. Table 2 presents useful characteristics for both materials.
Change in optical length for light with wavelength λ1 passing two windows each of thickness Lw due to change in temperature is

$$\Delta l_{\lambda 1} = 2[n_{\lambda 1}\alpha + (dn/dT)_{\lambda 1}]\Delta T \, Lw. \quad (7)$$

The uncompensated thermal phase shift is

$$\Delta\varphi = 2\pi( \Delta l_{\lambda 2} - \Delta l_{\lambda 1} )/ \lambda 1. \quad (8)$$

These expressions give for Lw=1.5 cm, ΔT=1°C for ZnSe the following shifts·

$\Delta\varphi_{(1.05\text{-}10.6)}$ = 0.166 rad., for λ1=10.6 μm and λ2=1.05 μm

and $\Delta\varphi_{(3.4\text{-}10.6)}$ = 0.055 rad. for λ1=10 6 , λ2=3.4 μm.

The later phase shift includes factor (1-x), introduced in section [4] A, taking into account the decrease in sensitivity for relatively close frequencies in this case $BaF_2$ has lower value of dn/dT and negative sign of the derivative. That leads to fractional compensation of the thermal expansion term and results in considerable less uncompensated phase shift. Is is more convenient to use 9-μm band for $CO_2$ laser output here because of larger absorption for 10μm band in $BaF_2$.

$\Delta\varphi_{(1.05\text{-}9.3)}$ = -0.0055 rad. for λ1= 9.3μm and λ2=1.05 μ.m

This uncompensated phase error can be expressed as fraction of the maximal phase shift in plasma:

$\Delta\varphi_{(1.05\text{-}10.65)}$ = 15%; $\Delta\varphi_{(3.4\text{-}10.6)}$ = 5% for ZnSe

and $\Delta\varphi_{(1.05\text{-}9.3)}$ = 0.42% for $BaF_2$, both for ΔT=1°C

It is clear from the above that keeping temperature of the windows constant or to control the temperature profile are very important for the reliable operation of the interferometer. In case of equal for two windows increase in temperature uncompensated phase shift substantially lower for $BaF_2$. Under plasma experiment the ECR heating will be used on LHD. Near the windows the microwave power density at 140GHz can reach 0.6 $W cm^{-2}$ that corresponds to absorbed 0.06 $W cm^{-3}$ in ZnSe according to date from

Table 2 . It is interesting that about the same heating load is expected from plasma emission. Extrapolation of bolometric data [34] to 10 MW heating power results in the total plasma emission power of 3 MW and in 0.6 $W{\cdot}cm^{-2}$ near the windows. It is possible to estimate temperature distribution across a window for given homogeneous voluminous heating. Figure 4 presents such a distribution for steady state and square ZnSe window when only microwave heating is included. The window is cooling from the edge where temperature is constant. This pillow-like distribution leads to corresponding distortion of wave front that will mask the modification of the phase shift produced by plasma. . The characteristic time scale for establishing the steady state is 1-1.5 minutes for dimensions of the $CO_2$ windows on LHD. We have no data about details of plasma emission as well as for $BaF_2$ absorption in the millimeter waves. The crucial issue for window is the safety factor in respect to vacuum breaking in the device. A larger friability of crystalline $BaF_2$ may be critical in deciding on window material. The ZnSe windows supplied with interferometric control of the phase shift caused by thermal effects are safer and could be the best choice.

B. Diffraction influences

Besides the time domain frequency dispersion in refractive materials there is an effect of dispersion for spatial frequencies of the probe beam when the beam travels in free space – diffraction phenomenon. Diffraction modifies the beam amplitude and phase profiles so its impact on the imaging with the slab probe beam is important and cannot be compensated automatically especially in a steady state operation. We consider below two diffraction effects.

*1.Beam shape.*

Diffraction at the beam aperture can disturb smoothness of probe beam while it travels over a long pass. The Gaussian beam is ideal to avoid distortion due to diffraction but sometimes it appeared not effective enough in filling the window aperture. A wider beam is preferable because a *k*-resolution is directly proportional to the beam size in plasma as it follows from the equation (6). It is usable to expand initially almost circular Gaussian beam by means of 1D-parabolic mirrors Instead of Gaussian shape a super-Gaussian one can be used [35, 36], which enables more effective filling of the aperture Another question is how to form a supper-Gaussian slab beam. One of the possible solutions is to cut a desired fraction from an over-expanded beam by means of "soft" apertures placed near or at the windows. The word "soft" means here –aperture with gradually increasing transmission from the edge to the center of the aperture. Such kind of apertures is convenient in high power laser technique to avoid damage of the laser rods by increased intensity in the diffraction pattern [35]. Variable reflectivity mirrors are used as soft apertures for $CO_2$ lasers [36], also non-axisymmetric apertures are employed to smooth the diffraction pattern at $\lambda = 10$ μm [37]. Smoothness of the beam phase profile is critical for homodyne interferometers to keep relative phase at maximal sensitivity over the entire beam cross-section. Heterodyne technique ensures continuous self-calibration of each spatial channel, still here it is possible to confuse a diffraction produced phase shift with that produced by plasma in case of variation of diffraction pattern during experiment, for example, due to vibrations. To exemplify it we consider the diffraction pattern of four types of the initial beam profiles: three of them are expressed by function

$$E`(x) = E_o \exp(-x/x_o)^q, \qquad (9)$$

where q = 2 for Gaussian beam , q = 6 for super-Gaussian one and the fourth beam is a plane wave. All beams pass through a linear aperture with clear width 2D = 5 cm. Figure 5 presents the initial electric field distribution of two Gaussian beam with $x_o/D$ = 0.55 and 0.93 and a super-Gaussian with xo/D = 0.82. The super-Gaussian beam has the same amplitude with one of the Gaussian beams at the edge of the aperture- 4% of the maximum and the same beam width at half maximum with the second Gaussian beam. All the beams have a waist at the aperture so the beam phase profile is initially flat. The waist length (Rayleigh length) $z_R = \pi xo^2/4\lambda \approx$ 200 m is much longer than all paths in the interferometer so the particular location of the beam waist is not crucial. Figures 6-13 represent the amplitude and phase profiles distribution versus distance from the aperture for four beams. The distributions are obtained by numerical calculation of Fresnel- Kirchhoff integral [38]

$$E(x,z) = \frac{1}{i\cdot\lambda\cdot z}\cdot\exp\left(i\cdot\pi\cdot\frac{x^2}{\lambda\cdot z}\right)\cdot \int_{-D/2}^{D/2} E`(v)\cdot\exp\left(-\frac{i\cdot\pi\cdot v\cdot(2\cdot x - v)}{\lambda\cdot z}\right)dv \qquad (10)$$

There is seen a sharp diffraction pattern with larger amplitude for larger modification of the initial beam produced by the aperture. The smaller the beam amplitude at the edge of the aperture the smoother profiles of the beam traveling behind the aperture. The phase profiles were plotted with negative sign for better visualization of details. The super-Gaussian beam ( plot 2 in Fig. 5) shows about as uniform profiles as the Gaussian one but is 70% wider than it. The diffraction patterns appeared strongly dependent on the initial beam shape.

It should be recognized though second color beam does not suffer from phase shape distortion due to diffraction it can be disturbed by ZnSe optics, which is difficult to produce with quality suitable for near

infrared interferometer. The difference in the shape of wave fronts for two colors may lead to imperfect compensation of vibrations by two color arrangement and to limitation in sensitivity of the interferometer in case of large vibrations.

*2 Diffraction impact on field depth of imaging techniques*

An important question is the role of diffraction in imaging of long phase objects. In imaging techniques lens relies precisely enough a thin phase object into the image plane (Fig.14). A problem arouses with a thick object or two objects separated by some distance $\Delta z$, which is usually the case in fusion plasmas diagnostics. Diffraction produced by an object located out of the subject plane generates parasitic amplitude modulations in the image plane that can deteriorate the phase modulation signal. A qualitative estimation of tolerable longitudinal size $\Delta z$ of a phase object can be obtained from Klein and Cook condition for a phase grating to be thin [39] $\Delta z_{max}(\Lambda) << \Lambda^2/(2\pi\lambda) =$ 160 cm for transverse size of fluctuations $\Lambda = 1$ cm and for $CO_2$ laser light. More precise treatment was performed in publications [40, 41].

Most publications on the role of diffraction in the imaging systems consider for simplicity harmonic phase modulation by a thin phase object translatable along the viewing direction [12, 40,41]. B.W. James and C.X. Yu [40] did not included in the treatment a reference beam and have found a homodyne signal in the image plane. This signal represents an amplitude modulation and is parasitic for imaging of a phase object hence it should be eliminated. J. Howard and L.E. Sharp [41] calculated both amplitude and phase modulation signals. The plot in Figure 15 shows the homodyne (amplitude) signal for three different wavelengths of plasma waves versus distance $\Delta z$ of the wave from the subject plane. Solid and doted curves represent calculations according to references [40] and [41] correspondingly. The results correlate with each other and show substantial increase in the amplitude signal with wave separation from the object plane and with decrease in the wavelength of fluctuations. The phase signal itself is practically independent of wave position along the probe beam unless its wavelength is considerable less than 1 cm (Fig.16.). The behaviour of the ratio of phase to amplitude signal $I_{ph}/I_{am}$ is determined mostly by variation of the amplitude signal as it shown in Figure 17 where $I_{ph}/I_{am}$ is plotted for different wavelengths of fluctuations according to publication [41]. The ratios decrease inversely proportional to the separation of modulations from the object plane and decrease as a square power of inverse wavelength of modulations These results confirms the qualitative estimation for the permissible longitudinal size of the observational zone: $\Delta z << \Delta z_{max}$. It follows herefrom limitation for wavelengths of phase fluctuations $\Lambda > 1$cm to prevent disturbances of the phase signal for the vertical viewing length of the LHD plasma of 160 cm

**[6] Bench top experiments**

To examine some of key points of the project bench top experiments were performed. Figure 18 shows schematic view of bench top experiments. We used a 15W $CO_2$ laser (MPB, GN-802-GES), an 1mW stabilized HeNe laser (MELES GRIOT) for the laser sources. For $CO_2$ laser detection, we employed a room temperature photovoltaic single detector for the reference chord and a room temperature photoconductive 10ch linear array detector for the slab beam detection (VIGO, PCI and PDI series). For HeNe laser detection, we used avalanche photodiodes (HAMAMATSU, C5331-03). Heterodyne intermediate frequency is 1MHz for both $CO_2$ and HeNe laser and acoustic optical modulator (Interaction Corp. model AGD-406B1 for CO2 laser and ISOMET CORP. model 1201E for HeNe laser produces it). The beam expander formed a 220mm 1/e2-intensity full width beam. The transmitting optics and the detection optics are placed 11m apart to simulate the same situation on LHD. Both transmitting bench and detection bench are on the gas springs in order to minimize mechanical vibration.

A. Spatial resolution

Figure 19 shows horizontal (x direction in Fig. 18) beam profile, which is measured 9.9m away from PM1. This position is the object plane. As shown in Fig.18, the beam, which is injected to PM1, is shifted horizontally. This is in order to check the effect of the aperture diffraction on the spatial resolution. Over-expanded beam would be useful in order to cover the whole area of the ports. Since lens or mirrors, which expanded the beam over the entire PM1, were not available, we checked this effect by shifting of the probe beam. Some structures are visible in beam edge due to the aperture effects as shown in Fig.19.

The spatial resolution was checked as follows. A thin teflon sheet (25μm thickness), of which width was 4mm, was scanned horizontally (along x direction) within narrow limits centered in either of two positions 1 and 2 across the slab beam (see Fig. 19). Three different locations along beam axis (different z position) are used also to check the field depth. One is 750mm ahead of the object plane, the second one is the object plane, and the third one is 640mm behind the object plane as shown in Fig.18. The distance between object plane and PM2 are the same as separation of plasma center and parabolic mirror on the top of the stand shown in Fig.1. These three positions roughly correspond to the top, center and bottom of LHD plasma. The linear array detector (D1) is placed to get a clear

image of the object plane. This position of D1 was determined and confirmed from the image of incoherent light source placed in the object plane.

Figures 20 shows measured phase profile of teflon object. The relative phase difference between edge channel of the detector array (here, we call ch1) and the other edge channel (here, we call ch10) was measured by the phase counter. When the phase image of the object passes ch1, the relative phase becomes positive and when it passes ch10, the relative phase becomes negative as shown in Figs.20.

The distance of the two peaks in Figs.20 corresponds to the separation of the ch1 and ch10 divided by the demagnification of the detection optics and the width of peaks corresponds to the width of the teflon object. As shown in Figs.20, the measured width of phase object does not exceed 4mm at any position. These results show that the imaging system can get a reasonably good image and promise 4mm spatial resolution across the beam axis. Resolution of 5 mm/channel needs to employ for slab beam of 250-280 mm width 50ch - 60ch - linear detector array for each port instead of 10ch array used in the bench-top experiment

B. Compensation of the mechanical vibration

The vibration compensation by combining with 633nm heterodyne HeNe laser interferometer was tested. As shown in Fig.18, a HeNe laser light of the second color interferometer was combined with $CO_2$ laser beam, then two-color beams travel three branches of the interferometer (probe, reference and local) together. Figure 21(a) shows measured mechanical vibration of test bench by using both $CO_2$ and HeNe laser interferometer. Figure 21(b) shows subtraction of measured vibration of two interferometers. Although both $CO_2$ and HeNe interferometer shows almost same measured vibration, there remains about 0.3μm uncompensated components as shown in Figs.21. This 0.3μm uncompensated components corresponds to 0.18rad for $CO_2$ laser interferometer and is not negligible compared to the phase shift of $CO_2$ laser interferometer due to the bulk plasma, which is 2 rad. The following reasons of existence of residual vibration signal are possible. Firstly, the present optics was not optimized for visible light and produces distortion of wave front for second color. This difference in wave front shapes for two colors provides uncompensated components. Secondly, optical mount to hold parabolic mirror was sensitive to vibration. When some vibration absorption material was introduced in the mount, the vibration was significantly reduced. In addition, because of the difference in beam size of $CO_2$ and HeNe laser, both beams suffer from different effect of vibrations. We need further development to reduce uncompensated vibration components. However, we can expect improvements on LHD. The mechanical vibration on FIR optical stand (shown in fig.1) was already measured by a HeNe laser interferometer, and it was about 1μm in several seconds. This background vibration was much less compared to the present bench top experiments. It is due to stiff structure of optical stand frame and optical mounts and due to shields to protect optics from background sound. From Figs.21, uncompensated components are one tenth of the full amplitude of the vibration. Therefore, if we can expect uncompensated components one tenth of full amplitude of the vibration, it will be about 0.1μm on LHD, which corresponds to 0.018 rad or one hundredth of phase shift of bulk plasma.

C. Phase resolution

In order to check phase resolution, we measured the change of the refractive index of the air due to the ultrasonic waves. A 33.5kHz ultrasonic oscillator was placed on the reference path as shown in Fig.18, and the ultrasonic waves were injected vertically (along y direction). The phase difference between the reference beam and the slab beam was measured by using phase counter. Since background phase noise, which is mainly caused by the vibration, was much more significant than ultrasonic signal, we used band-pass filter around 30 kHz to get a signal with good SNR. Figure 22 shows comparison of the power spectrum of the phase counter output. With ultrasonic waves, very sharp peak, which corresponds to the resonant frequency of the ultrasonic oscillator, appeared. The phase signal amplitude of this ultrasound is about $5\times10^{-4}$ rad. As we described in section [4], we expect $3\times10^{-3}$ rad phase shift due to the fluctuation, therefore, present phase resolution will be enough to measure fluctuation. The time resolution of the present phase counters is about 200 kHz in order to keep good phase resolution. If more higher frequency components are dominant, we need further development time resolutions of phase counter keeping present phase resolution, or should try PCI schema for fluctuation measurements. Frequency response of PCI is determined by frequency response of the detector, which is several MHz.

## [7]. Conclusion

$CO_2$ laser based diagnostics of plasma density profile in regimes with the sharp density gradient is proposed. It has also capability to study plasma fluctuations with the same apparatus. Both imaging and scattering techniques are employed for observation of plasma fluctuation. There are still a few topics, which need additional study to install the diagnostics

## References

[1]. K. Kawahata, K. Tanaka, Y. Ito, A. Ejiri, S.Okajima, Rev. Sci. Instrum., 70, 707, (1999)

[2] N. Bretz, Rev. Sci. Instrum., 68, 2927, (1997)
[3] R A. Koch, W.M Tang, Phys. Fluids, 21, 1236, (1978)
[4] D.L. Brower et al., Rev. Sci. Instrum , 61, 3019, (1990)
[5]. C.L. Retting et al., Rev. Sci. Instrum., 66, 848, (1995)
[6]. K. L. Wong et al, Phys. letters, A276, 281, (2000)
[7] U. Stroth, Plasma Phys. Control. Fusion, 40, 9, (1998)
[8]. A.J. Donne, Rev. Sci. Instrum., 66, 3407, (1995)
[9]. V.D. Drachev et al., Rev. Sci. Instrum., 64,1010, (1993)
[10]. N. Bretz et al., Rev. Sci. Instrum., 68, 713, (1995)
[11]. H. Weisen, Plasma Phys. Control. Fusion, 28, 1147, (1986), H Weisen et. al., Plasma Phys. Control. Fusion, 30, 293, (1988),
[12]. K.Matsuo et al, Japanese Journal of Applied Physics, vol 30,p1102, (1991)
[13]. D.E. Evans et. al. Plasma Phys., 24, 834, (1982)
[14]. C.A.J. Hugenholtz, B.J.H. Meddens, Rev. Sci. Instrum., 53, 171, (1982)
[15]. K. Tanaka et al, Japanese Journal of Applied Physics, vol 31, p2260, (1992)
[16]. K. Tanaka et al, Journal of Physical Society of Japan, vol 62,p3092, (1993).
[17]. A. Truc et al., Rev. Sci. Instrum., vol. 63p.3716, (1992)
[18]. S.Kado et al, Japanese Journal of Applied Physics, vol 34, p6492, (1995)
[19]. S.Kado et al, Journal of Physical Society of Japan, vol 65,p3434, (1996)
[20]. C.M. Surko, R.E. Slusher, Phys. Fluids, 23, 2425, (1980)
[21]. B.A. Spivey et al., Rev. Sci. Instrum., 63, 5252, (1992)
[22]. Y. Kawano et al., Rev. Sci. Instrum., 67, 1520, (1996)
[23]. Y.Jiang et al, Rev. Sci. Instrum. 68, p902, (1997)
[24]. Y. Jiang et al., Rev. Sci. Instrum., 70, 703, (1999)
[25]. A. Truc et al., Rev. Sci. Instrum., 63, 3716, (1992)
[26]. R. Nazikian, L.E. Sharp, Rev. Sci. Instrum., 58, 2086, (1987)
[27]. E. Lo et al., Rev. Sci. Instrum., 68, 1206, (1997)
[28]. H.H. Li, J. Phys. Chem. Ref. Data, 13, 123, (1984)
[29]. H.H. Li, J. Phys. Chem. Ref. Data, 9, 226, (1980)
[30]. M. Stead, G. Simons, Appl. Optics, 28, 1874, (1989)
[31]. Handbook of Optics, McGRAW- Hill, N.Y., (1978)
[32]. Physical Constants, ed. I.S. Grigor'ev, E.Z. Meylikhov, Energoatomizdat), Moscow, (1991) (in Russian).
[33]. G.G. Gadzhiev, Ya.M. Shakhabudinov, Sov. J. Opt. Technol., 58, 302, (1991)
[34] B.J. Peterson et al., Proc of 26 EPS Conf on Contr. Fusion and Plasma Phys., ECA, 23J, 1337, (1999).
[35]. I. K. Krasyuk, S. G. Lukishova, P. P. Pashinin, A. M. Prokhorov, and A. V. Shirkov, Soviet J Quantum Electr., 6, 725, (1976)
[36] E. Galetti, D.V. Willetts, M.R. Harris, Appl. Opt., 36, 1269, (1997)
[37]. S. A. Dimakov, et al., Soviet J. Quantum Electr., 20, 231, (1990)
[38]. J.W. Goodman, Introduction to Fourier Optics, N.Y., McGraw-Hill, (1968)
[39]. W.R. Klein, B.D. Cook, IEEE Trans. Sonic Ultason., SU-14, 123, (1967)
[40]. B.W. James, C.X. Yu, , Plasma Phys. Control. Fusion, 27, 557, (1985)
[41]. J. Howard, L.Sharp, , Plasma Phys. Control. Fusion, 34, 1133, (1992)

**Figure Captions**

Fig1. Schematic view of $CO_2$ laser interferometer

Fig.2. Diagram of two-color $CO_2$ laser based diagnostics. Notations: AOM-acousto-optic modulator, D1-4, APD1-2-detectors for 10μm and 1 μm radiation respectivelly, , BEX- mirror beam expander, , PM- parabolic mirror, SP-calibrated high frequency speaker, PBS- polarization splitter for separation beams with orthogonal polarisation directions, BS-beam splitter, SL- slit,

Fig.3. Structure of the probe and the reference beams

Fig.4. Temperature distribution for steady state homogeneous voluminous heating of square window, cooled from the edge

Fig.5. Initial electric field distribution given by equation (9) at the plane of an linear aperture with width of 2D= 5 cm. Parameters of each distribution are indicated at the plots.

Fig.6-13. Diffraction of $CO_2$ laser beam at the linear aperture of width 2D.Amplitude (Fig.6, 8, 10, 12) and phase (Fig. 7,9,12,13) profiles distribution versus distance from the aperture for electric field distribution in the aperture plane shown in Figure 5. Diffraction patterns for a plane wave are presented in Figures 12,13.

Fig.14. Diffraction of collimated light beam on thin plasma waves in the context of imaging techniques

Fig.15. Homodyne signal in the image plane vs distance (in cm) of the phase screen from the object

plane for different wavelengths of modulations. Solid and doted curves represent calculations according to reference [40] and [41] correspondingly

Fig.16. Phase (heterodyne) signal versus density wave separation from the subject plane $\Delta z$ (see Figure 14). Wavelengths of the density waves are indicated at the curves.

Fig.17. Ratio of homodyne to heterodyne signal vs separation between the phase screen and the objection plane $\Delta z$ (see Figure 14) for the beam waist in plasma 3 cm

Fig.18 Schematic view of bench top experiment AOM; Acoustic Optical Modulator, PM1,PM2; off axis parabolic mirrors, D1,D2; detectors for $CO_2$ laser, APD1,APD2; Avalanche photodetector for HeNe laser, Cly; Cylindrical mirror. HeNe1 and HeNe 2 are for alignment, HeNe3 is for the second color interferometer. D1 are 10ch array detector, D2 is single detector. Focal lengths are shown in mm. Cylindrical mirror compresses beam in the y direction to increase the beam power density.

Fig.19 Beam profile of slab beam

Fig.20 Check of the spatial resolution from the measurement of the scanning teflon sheet for different z-location of the teflon sheet as it is shown in the Figure. Positions 1 and 2 for scanning teflon sheet are indicated in Fig. 4.

Fig.21 (a) Measured mechanical vibration (b) Uncompensated vibration, which is subtraction of $CO_2$ and HeNe laser interferometer data.

Fig.22 Power spectrum of ultrasonic (US) signal.

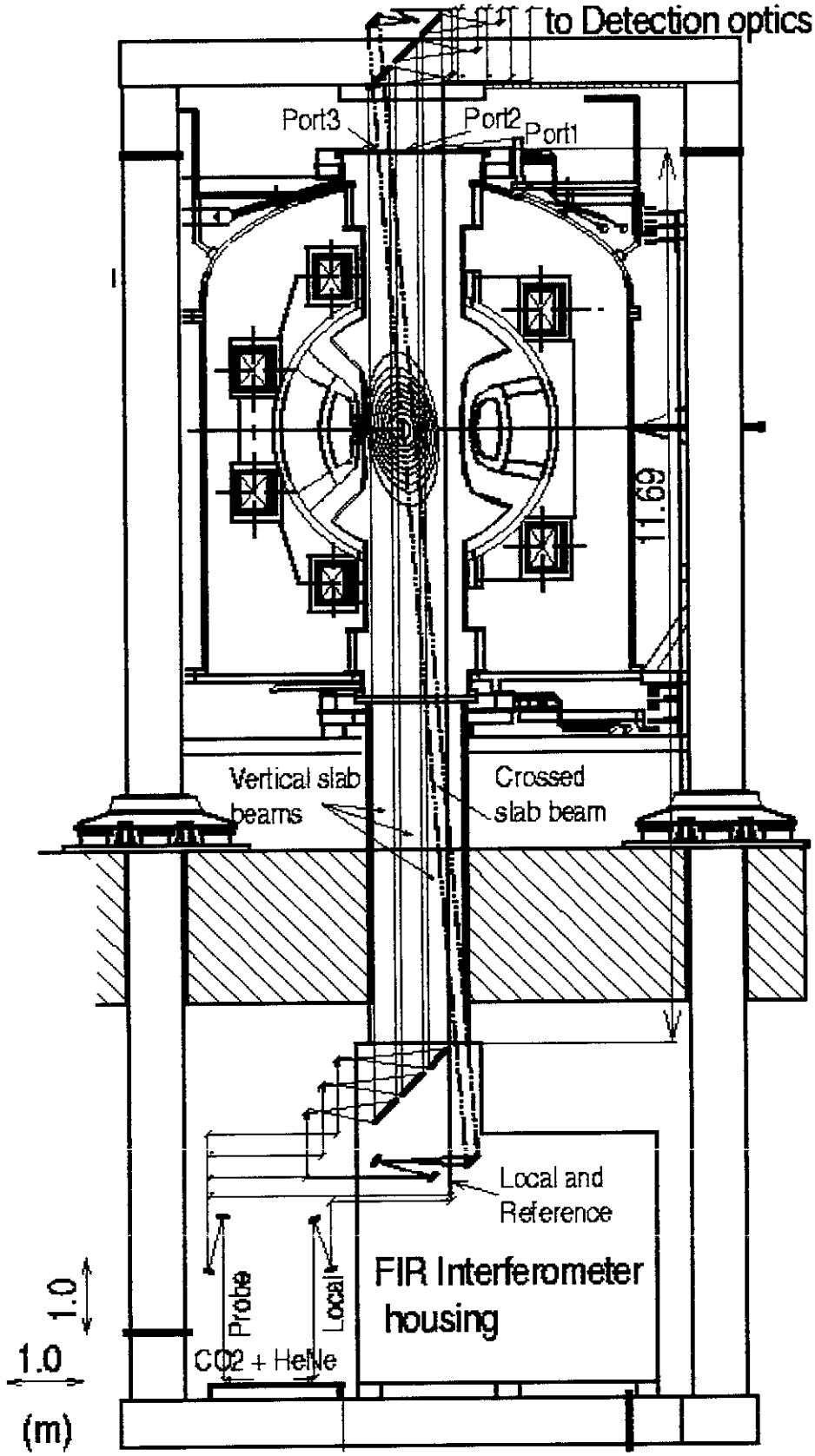
to Detection optics
Port3
Port2
Port1
11.69
Vertical slab beams
Crossed slab beam
Local and Reference
FIR Interferometer housing
Probe
Local
CO2 + HeNe
1.0
1.0
(m)

Fig. 1

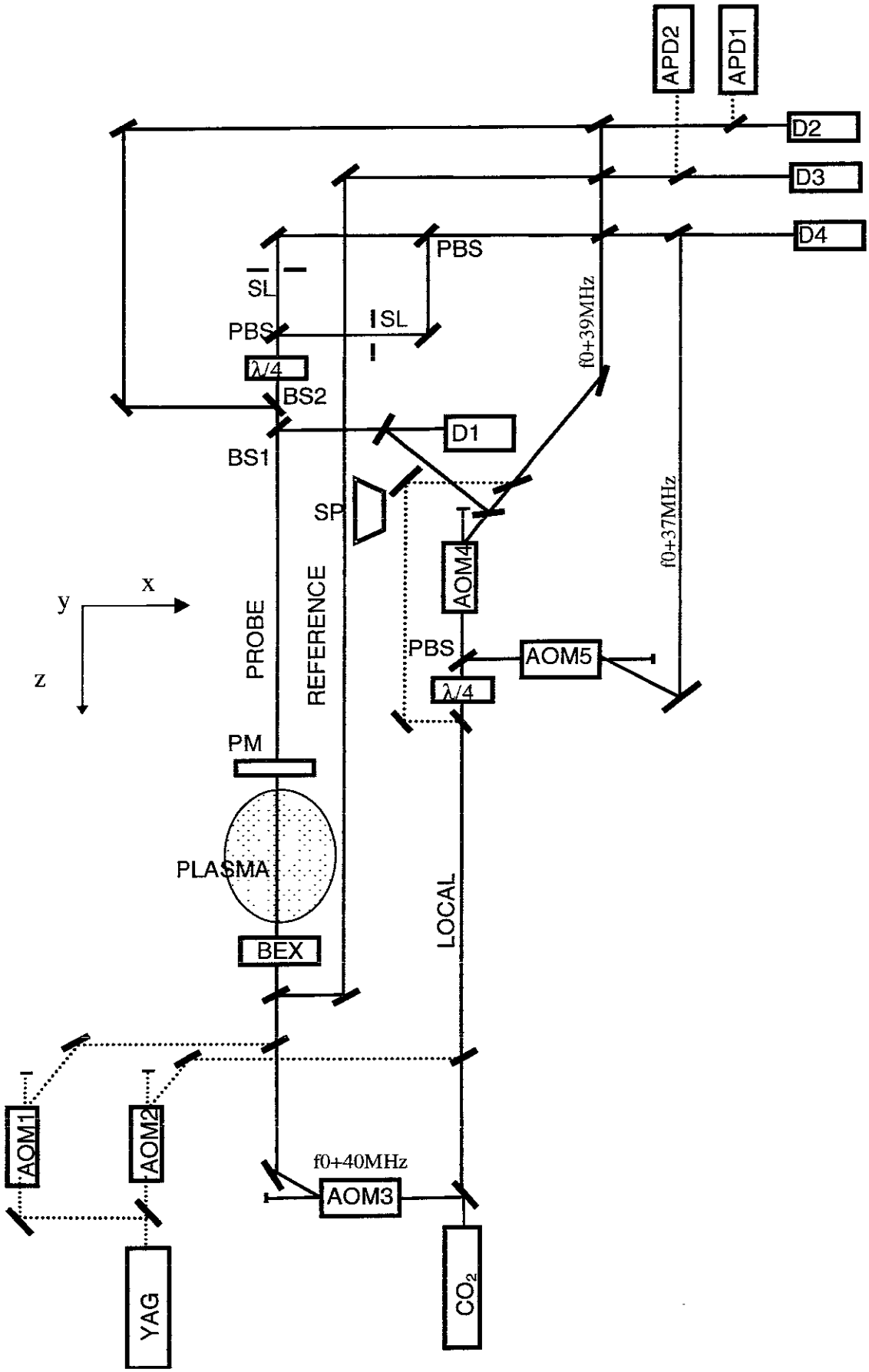
APD2
APD1
D2
D3
D4
PBS
SL
SL
PBS
λ/4
BS2
BS1
D1
f0+39MHz
f0+37MHz
SP
AOM4
PBS
AOM5
λ/4
y
x
z
PROBE
REFERENCE
PM
PLASMA
BEX
LOCAL
AOM1
AOM2
f0+40MHz
AOM3
YAG
$CO_2$

Fig. 2

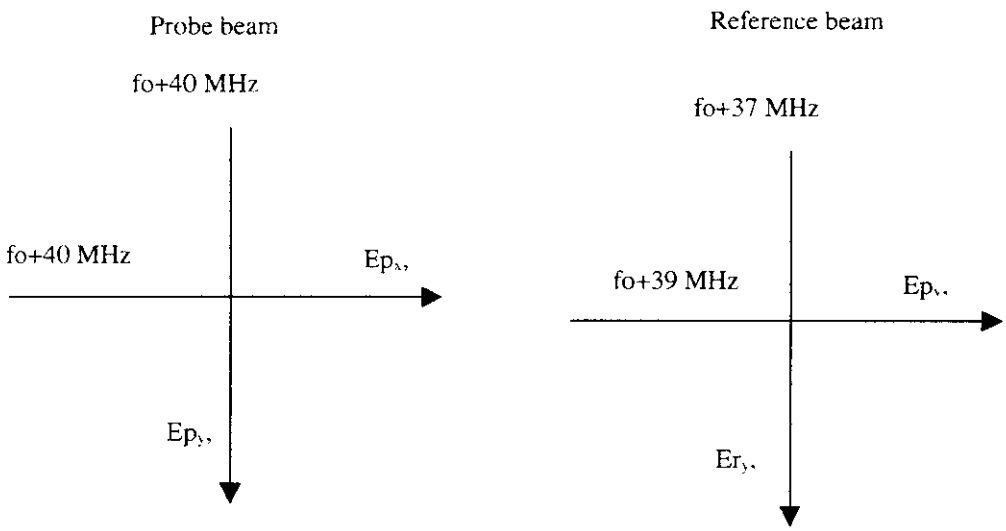
Probe beam
fo+40 MHz
fo+40 MHz
Epx,
Epy,
Reference beam
fo+37 MHz
fo+39 MHz
Epx,
Ery,

Fig.3

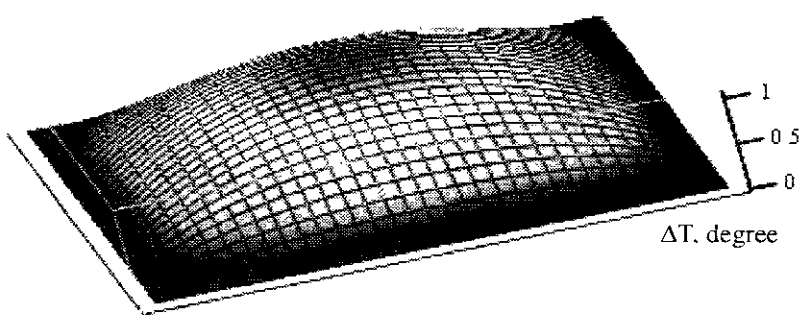
1
0 5
0
ΔT, degree

Fig. 4

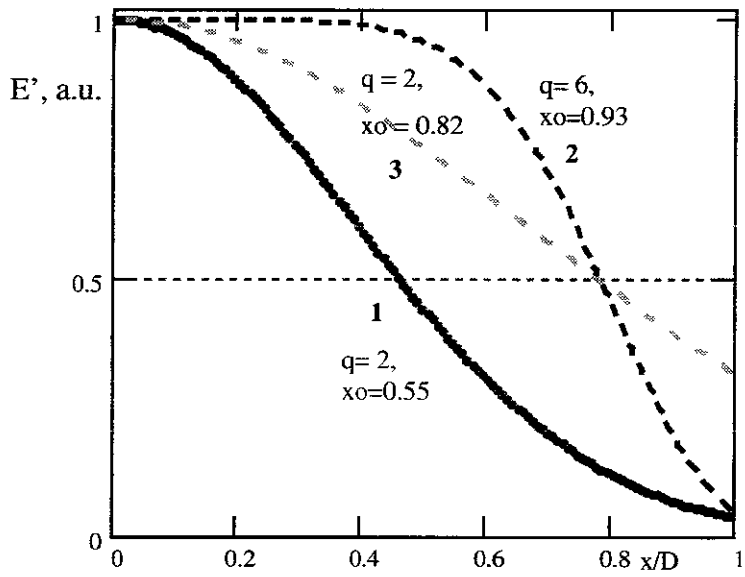


Fig. 5

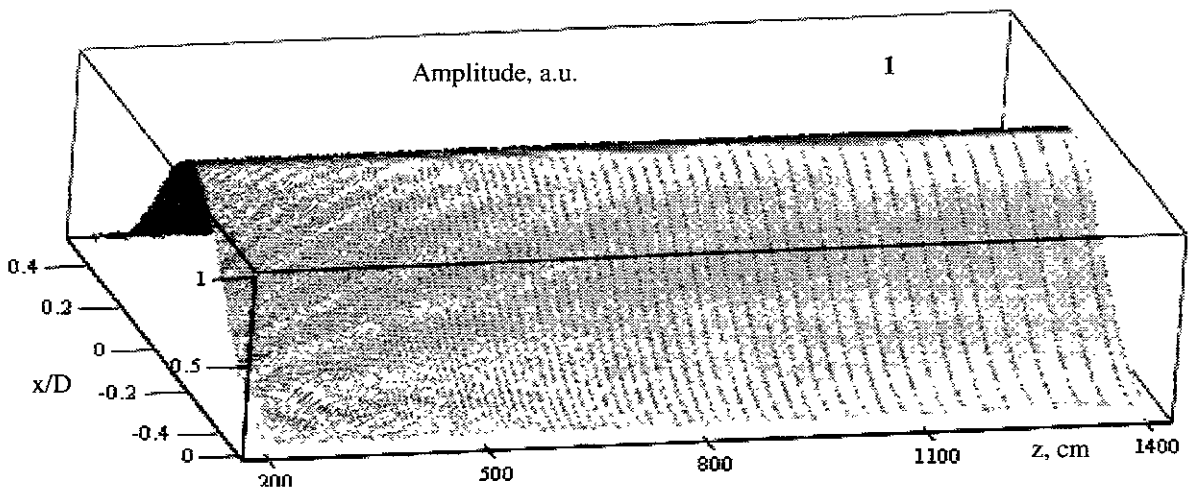


Fig.6.

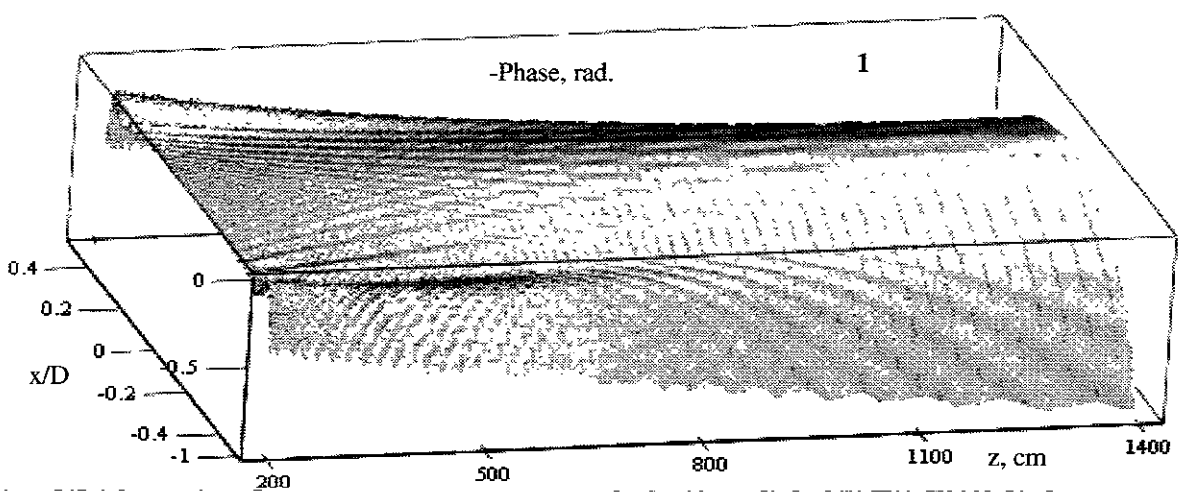


Fig.7.

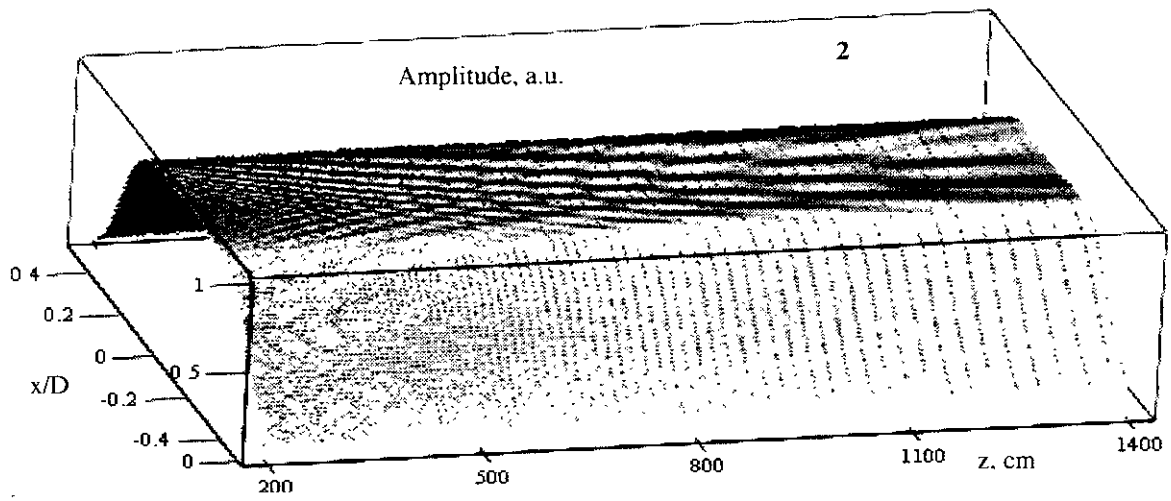


Fig.8.

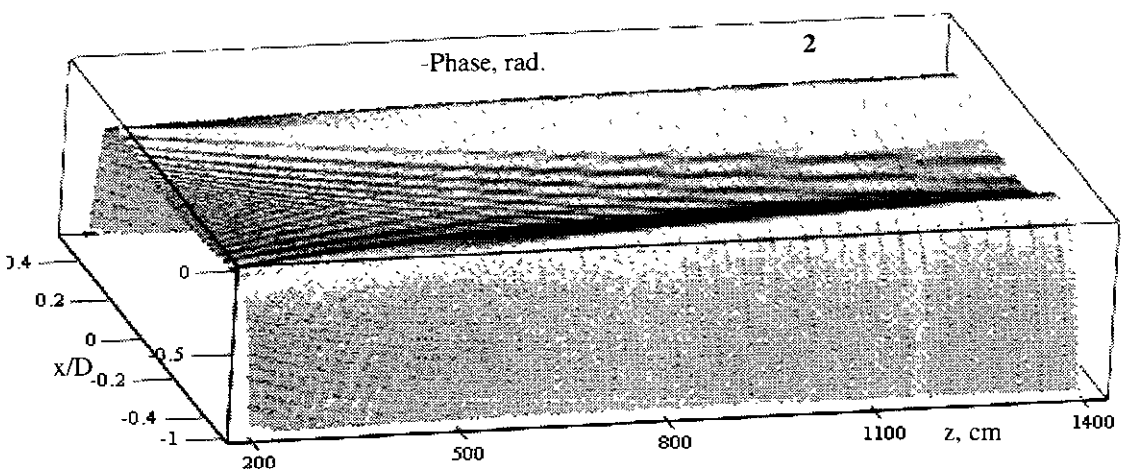


Fig.9.

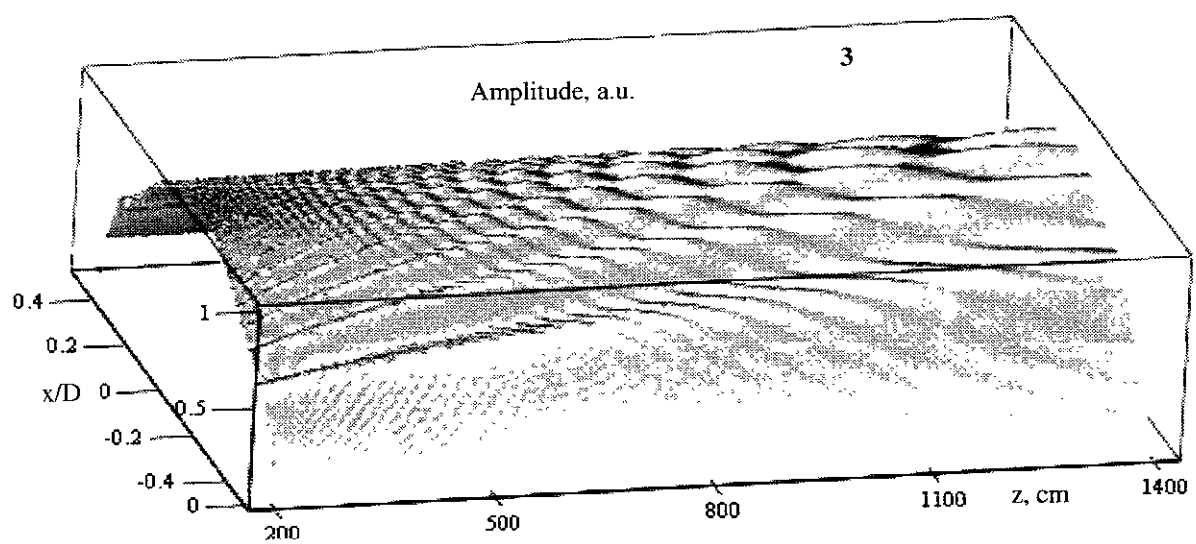


Fig.10.

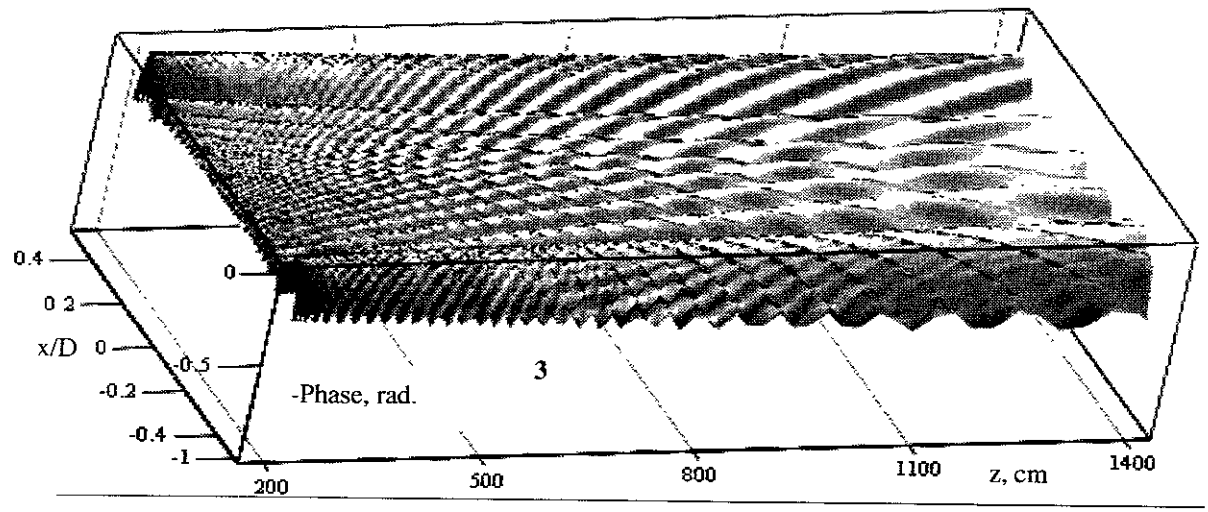


Fig.11.

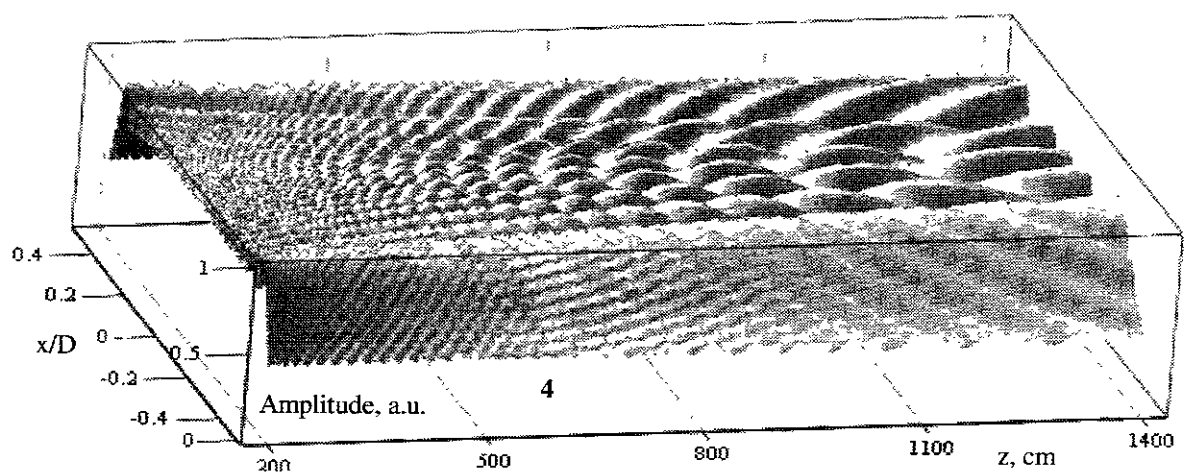


Fig.12.

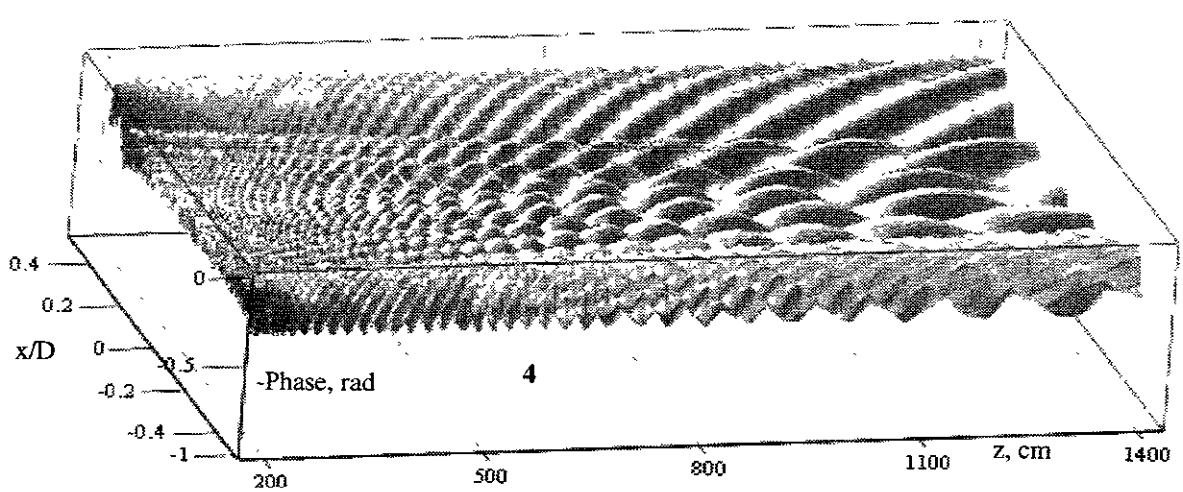


Fig.13

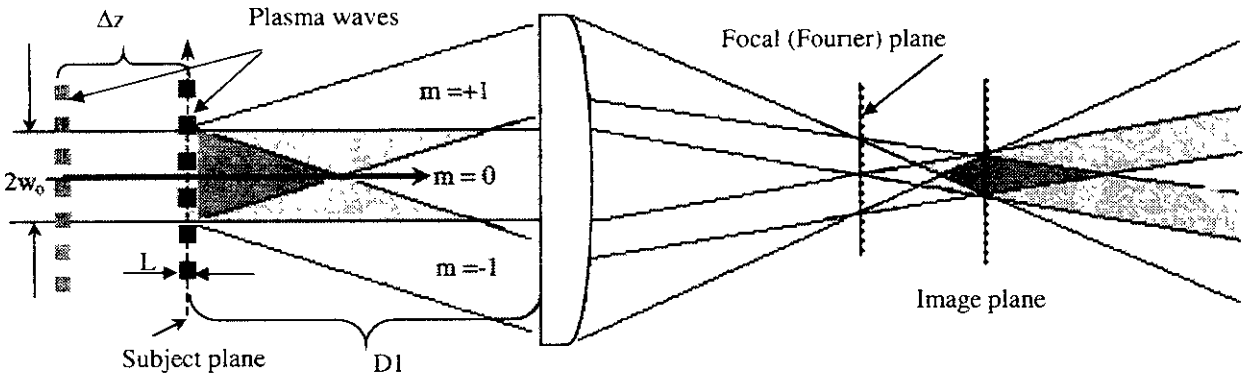


Fig.14

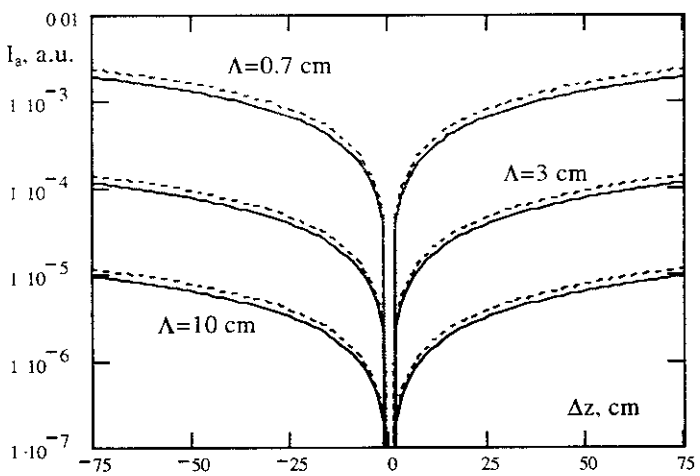


Fig.15.

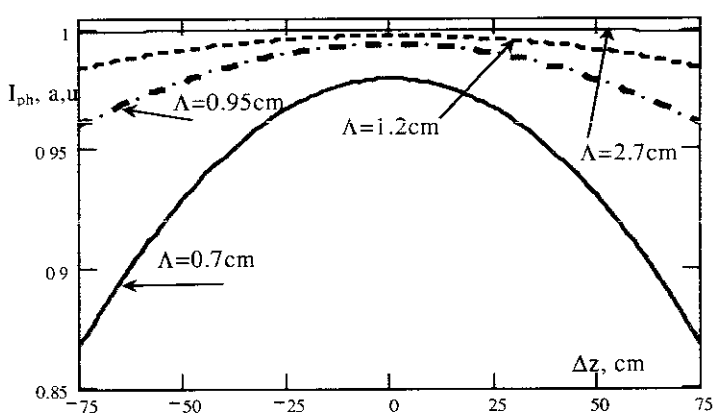


Fig.16.

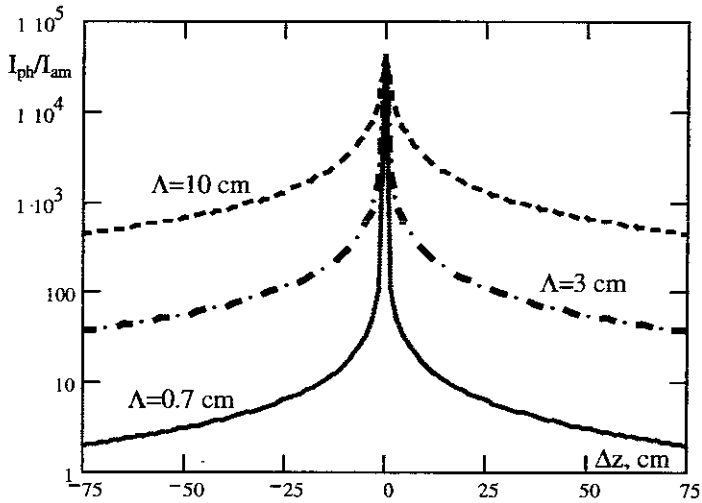
1 10^5
I_ph/I_am
1 10^4
1·10^3
100
10
1
Λ=10 cm
Λ=3 cm
Λ=0.7 cm
Δz, cm
-75
-50
-25
0
25
50
75

Fig.17.

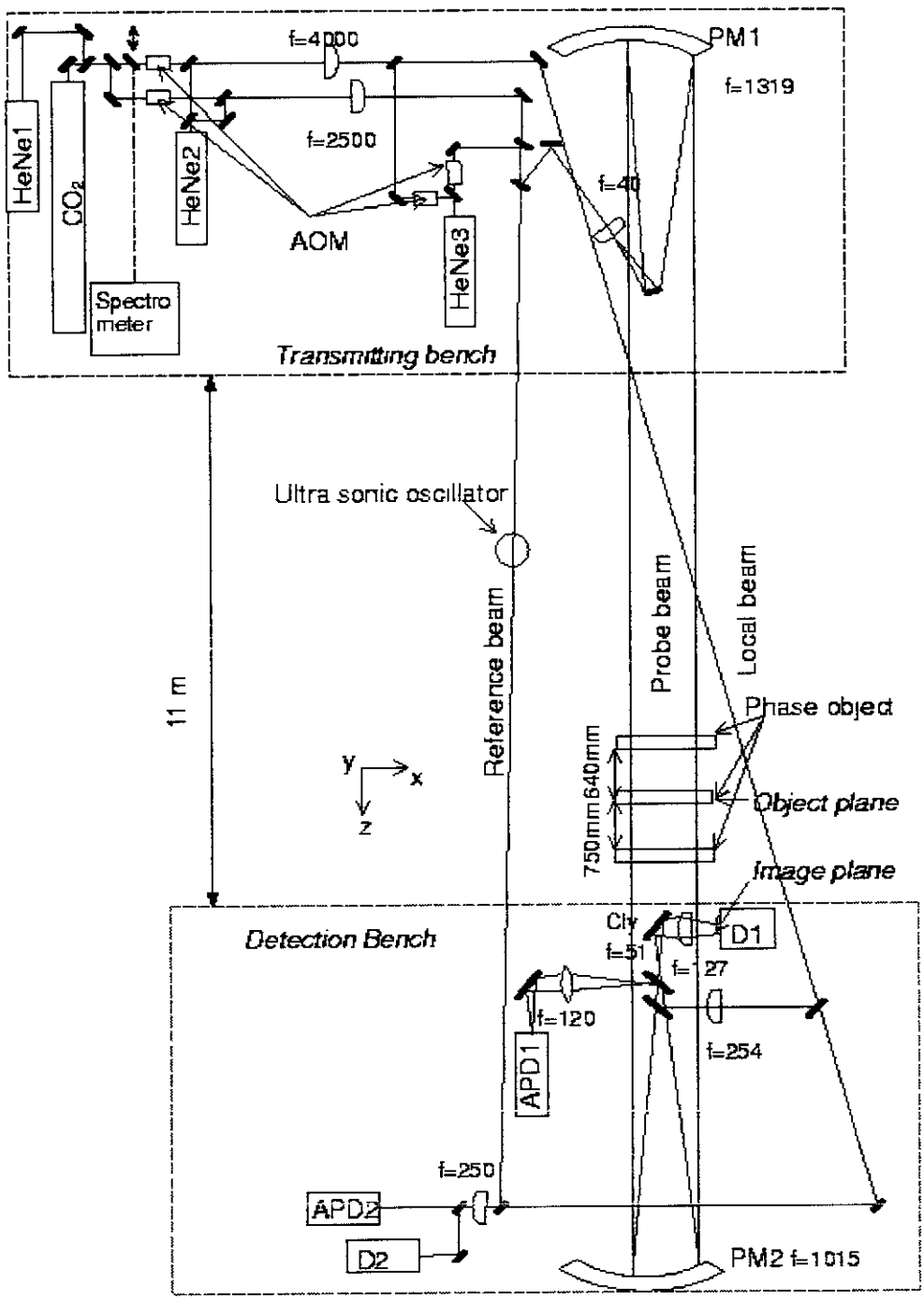
f=4000
PM1
f=1319
f=2500
HeNe1
CO2
HeNe2
AOM
HeNe3
f=40
Spectro meter
Transmitting bench
Ultra sonic oscillator
Reference beam
Probe beam
Local beam
11 m
Phase object
750mm 640mm
Object plane
Image plane
y
x
z
Detection Bench
Ch
D1
f=51
f= 27
f=120
APD1
f=254
f=250
APD2
D2
PM2 f=1015

.Fig. 18

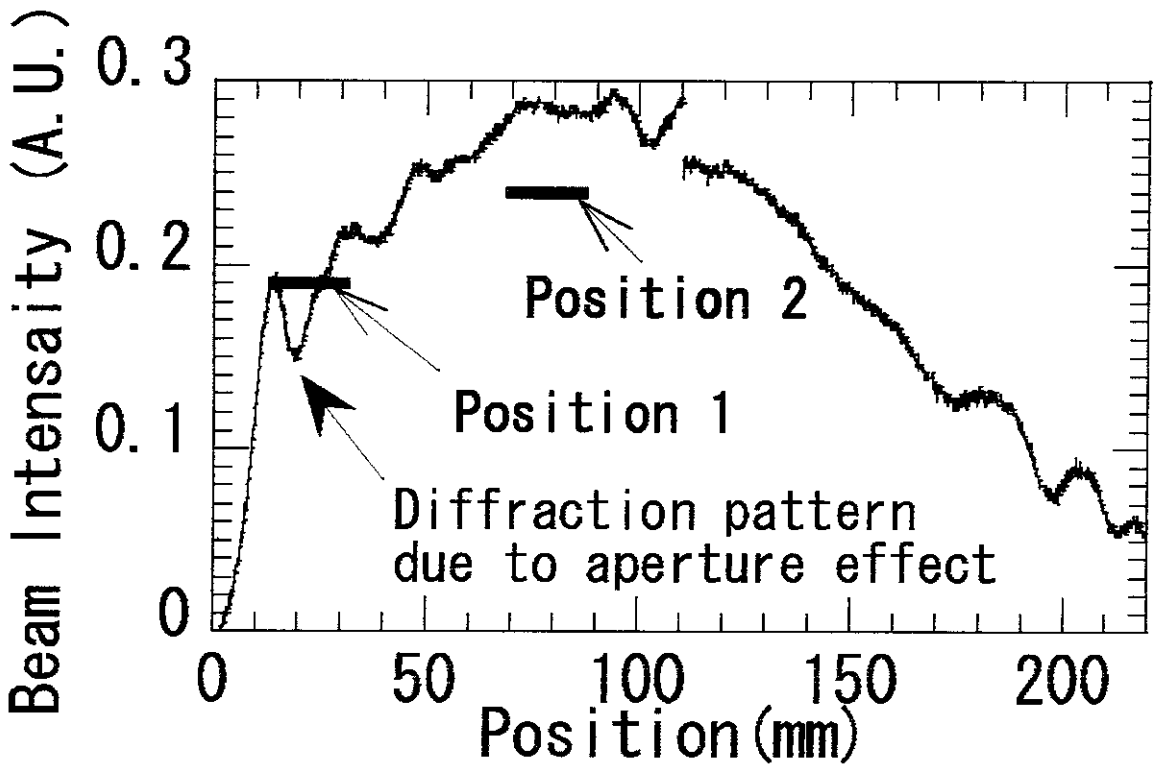
Beam Intensaity (A.U.)
0.3
0.2
0.1
0
0
50
100
150
200
Position(mm)
Position 2
Position 1
Diffraction pattern
due to aperture effect

Fig.19

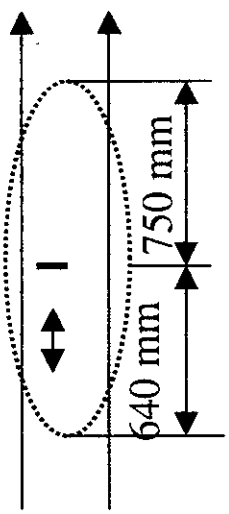
750 mm
640 mm

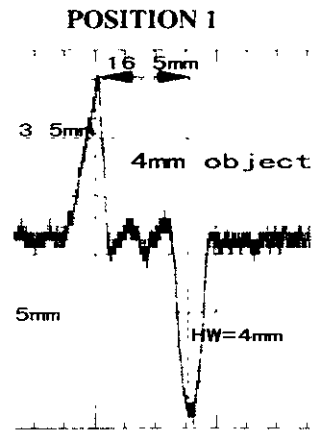
POSITION 1
16.5mm
3.5mm
4mm object
5mm
HW=4mm

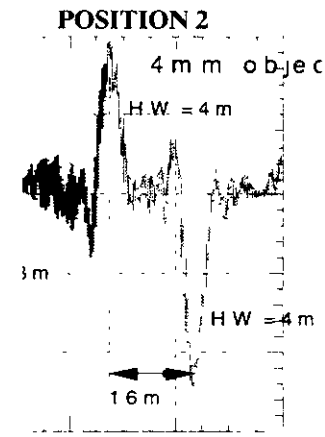
POSITION 2
4mm object
H.W.=4m
H.W.=4m
16m

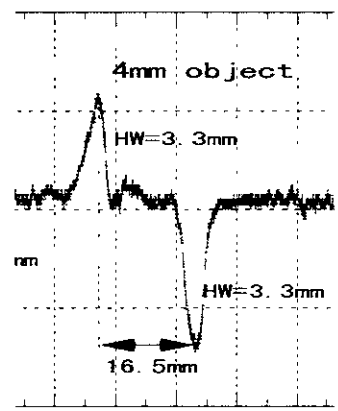
4mm object
HW=3.3mm
HW=3.3mm
16.5mm

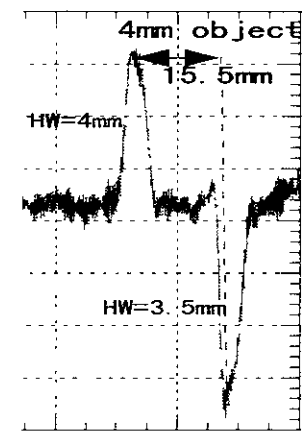
4mm object
15.5mm
HW=4mm
HW=3.5mm

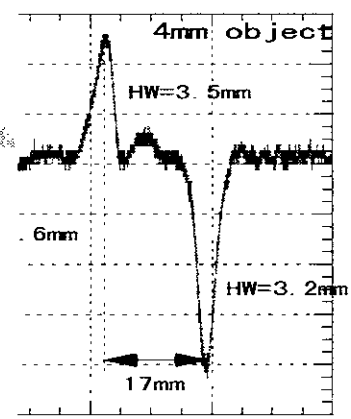
4mm object
HW=3.5mm
HW=3.2mm
17mm

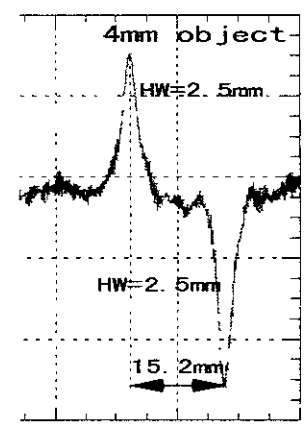
4mm object
HW=2.5mm
HW=2.5mm
15.2mm

Fig.20

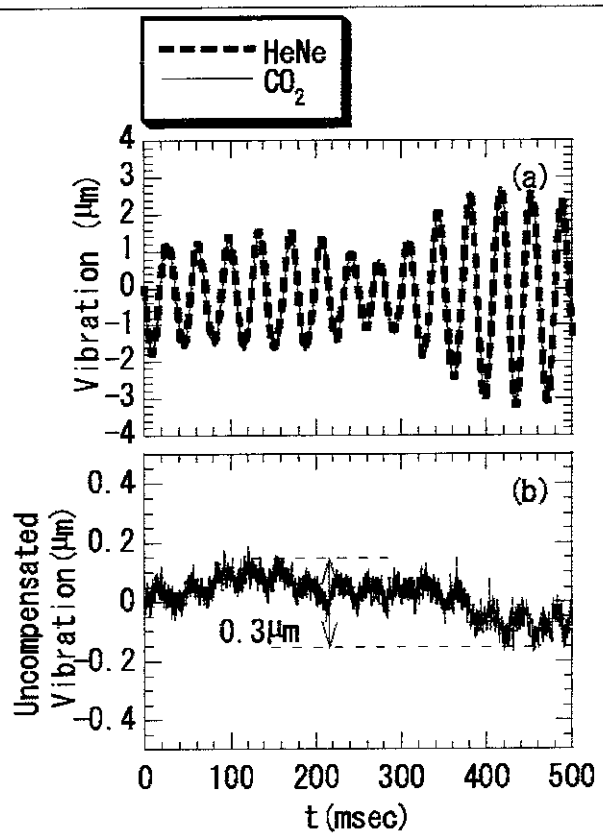
HeNe
CO2
(a)
(b)
Vibration (μm)
Uncompensated Vibration (μm)
0.3μm
t (msec)

Fig.21

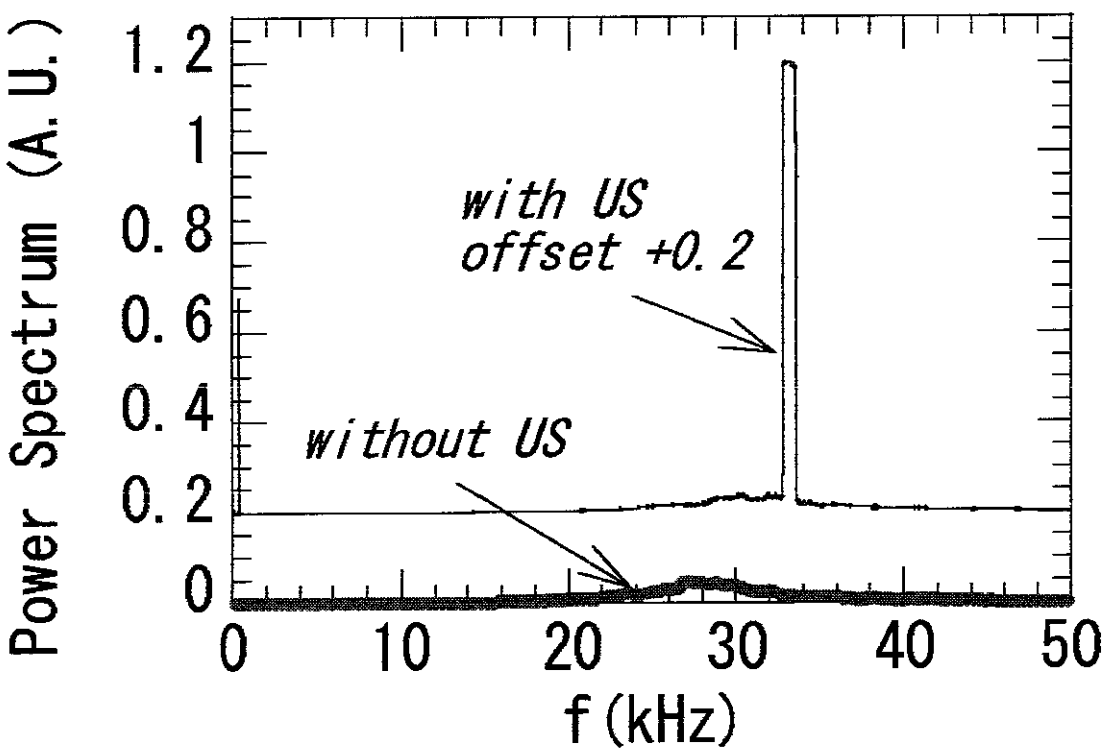
Power Spectrum (A.U.)
with US
offset +0.2
without US
f (kHz)

Fig.22

# Recent Issues of NIFS Series

NIFS 669 K Mima, M S Jovanovic, Y Sentoku Z-M Sheng, M M Skoric and T Sato
Stimulated Photon Cascade and Condensate in Relativistic Laser plasma Interaction Nov 2000

NIFS-670 L Hadzievski M M Skoric and T Sato,
On Origin and Dynamics of the Discrete NLS Equation Nov 2000

NIFS-671 K Ohkubo, S Kubo, H Idei T Shimozuma, Y Yoshimura F Leuterer, M Sato and Y Takita,
Analysis of Oversized Sliding Waveguide by Mode Matching and Multi Mode Network Theory Dec 2000

NIFS-672 C Das, S Kida and S Goto,
Overall Self-Similar Decay of Two-Dimensional Tirbulence Dec 2000

NIFS-673 L A Bureyeva T Kato, V S Lisitsa and C Namba,
Quasiclassical Representation of Autoionization Decay Rates in Parabolic Coordinates Dec 2000

NIFS-674 L A Bureyeva V S Lisitsa and C Namba,
Radiative Cascade Due to Dielectronic Recombination Dec 2000

NIFS-675 M FHeyn, S V Kasilof, W Kernbichler, K Matsuoka, V V Nemov, S Okamura, O.S Pavlichenko
Configurational Effects on Low Collision Plasma Confinement in CHS Heliotron/Torsatron, Jan 2001

NIFS-676 K Itoh,
A Prospect at 11th International Toki Conference - Plasma physics, quo vadis?, Jan 2001

NIFS-677 S Satake, H Sugama, M Okamoto and M Wakatani,
Classification of Particle Orbits near the Magnetic Axis in a Tokamak by Using Constants of Motion Jan 2001

NIFS-678 M Tanaka and A. Yu Grosberg,
Giant Charge Inversion of a Macroion Due to Multivalent Counterions and Monovalent Coions Molecular Dynamics Studyn, Jan 2001

NIFS-679 K Akaishi, M Nakasuga, H Suzuki, M Iima, N Suzuki, A Komori, O Motojima and Vacuum Engineering Group,
Simulation by a Diffusion Model for the Variation of Hydrogen Pressure with Time between Hydrogen Discharge Shots in LHD, Feb 2001

NIFS-680 A Yoshizawa, N Yokoi, S Nisizima, S -I Itoh and K Itoh
Variational Approach to a Turbulent Swirling Pipe Flow with the Aid of Helicity, Feb 2001

NIFS-681 Alexander A.Shishkin
Estafette of Drift Resonances, Stochasticity and Control of Particle Motion in a Toroidal Magnetic Trap, Feb 2001

NIFS-682 H Momota and G H Miley,
Virtual Cathode in a Spherical Inertial Electrostatic Confinement Device, Feb 2001

NIFS-683 K Saito, R Kumazawa, T Mutoh, T Seki, T Watari, Y Torii, D A Hartmann, Y Zhao, A Fukuyama, F Shimpo, G. Nomura, M Yokota, M Sasao, M Isobe, M Osakabe, T Ozaki, K Narihara, Y Nagayama, S Inagaki, K Itoh, S Morita, A V Krasilnikov, K. Ohkubo, M Sato, S. Kubo, T Shimozuma, H Idei, Y Yoshimura, O Kaneko, Y Takeiri, Y Oka, K Tsumori, K Ikeda, A Komori, H Yamada, H Funaba, K Y Watanabe, S Sakakibara, M Shoji, R Sakamoto, J Miyazawa, K Tanaka, B J Peterson, N Ashikawa, S Murakami, T Minami, S Ohakachi, S Yamamoto, S Kado, H Sasao, H Suzuki, K Kawahata, P deVries, M Emoto, H Nakanishi, T Kobuchi, N Inoue, N Ohyabu, Y Nakamura, S. Masuzaki, S Muto, K Sato, T Morisaki, M Yokoyama, T Watanabe, M Goto, I Yamada, K. Ida T. Tokuzawa, , N Noda, S Yamaguchi, K Akaishi, A Sagara, K Toi, K Nishimura, K. Yamazaki, S Sudo Y. Hamada, O Motojima, M Fujiwara,
Ion and Electron Heating in ICRF Heating Experiments on LHD Mar 2001

NIFS-684 S Kida and S Goto,
Line Statistics Stretching Rate of Passive Lines in Turbulence Mar 2001

NIFS-685 R Tanaka, T Nakamura and T Yabe,
Exactly Conservative Semi-Lagrangian Scheme (CIP-CSL) in One-Dimension Mar 2001

NIFS-686 S Toda and K Itoh,
Analysis of Structure and Transition of Radial Electric Field in Helical Systems Mar 2001

NIFS-687 T Kuroda and H Sugama,
Effects of Multiple-Helicity Fields on Ion Temperature Gradient Modes Apr 2001

NIFS-688 M Tanaka,
The Origins of Electrical Resistivity in Magnetic Reconnection Studies by 2D and 3D Macro Particle Simulations Apr. 2001

NIFS-689 A Maluckov, N Nakajima, M Okamoto, S Murakami and R Kanno,
Statistical Properties of the Neoclassical Radial Diffusion in a Tokamak Equilibrium Apr 2001

NIFS-690 Y Matsumoto T Nagaura, Y Itoh, S-I Oikawa and T Watanabe,
LHD Type Proton-Boron Reactor and the Control of its Peripheral Potential Structure Apr 2001

NIFS-691 A Yoshizawa, S -I Itoh, K. Itoh and N Yokoi,
Turbulence Theories and Modelling of Fluids and Plasmas Apr 2001

NIFS-692 K. Ichiguchi, T Nishimura, N Nakajima M Okamoto, S -i Oikawa M Itagaki,
Effects of Net Toroidal Current Profile on Mercier Criterion in Heliotron Plasma Apr 2001

NIFS-693 W Pei, R Horiuchi and T Sato
Long Time Scale Evolution of Collisionless Driven Reconnection in a Two-Dimensional Open System, Apr. 2001

NIFS-694 L N Vyachenslavov, K Tanaka K Kawahata,
CO2 Laser Diagnostics for Measurements of the Plasma Density Profile and Plasma Density Fluctuations on LHD Apr 2001